**Supporting Information to**

# Tannin-based resins for 3D printing of porous carbon architectures

*Pauline Blyweert †, Vincent Nicolas †, Jan Macutkevic‡ ,*

*Vanessa Fierro †, Alain Celzard †,**

† Université de Lorraine, CNRS, IJL, F-88000 Epinal, France

‡ Faculty of Physics, Vilnius University, Sauletekio 9, LT-10222 Vilnius, Lithuania

**Number of pages: 10**

**Number of tables: 6**

**Number of figures: 6**

**Structural and textural properties**

*Corresponding author: Pr. Alain Celzard (alain.celzard@univ-lorraine.fr) Université de Lorraine

*XRD*

The size of the coherent domain along the *a* axis ($L_{a,\ XRD}$) was calculated from the *10*λ reflection using the modified Scherrer equation [1,2]:

$$L_{a,XRD} = \frac{K\lambda}{B\cos\theta} \quad \text{(S1)}$$

where *K* is a factor equal to 1.85, $\lambda$ (nm) is the radiation wavelength (here 0.15406 nm), $\theta$ (rad) is the Bragg angle, and *B* is the full width at half maximum (FWHM) of the reflection.

*Raman spectroscopy*

The crystallite size $L_{a,\ Raman}$ (nm) was deduced from the half-width at half maximum of the G band, $HWHM_G$ ($cm^{-1}$), according to Eq. (S2) [3]:

$$HWHM_G = (68 \pm 4) - (5.2 \pm 0.5)\ L_{a,\ Raman} \quad \text{(S2)}$$

which is valid for $L_{a,\ Raman}$ below ~ 10 nm, a situation that will be shown to apply to the highly disordered carbons discussed here.

*Mercury porosimetry*

The pore entrance diameter, *D* (m), was calculated by application of Washburn's equation:

$$D = -\frac{4\gamma\cos\varphi}{P} \quad \text{(S3)}$$

where $\gamma$ (480 mJ $m^{-2}$) is the surface tension of mercury, $\varphi$ (140°) is the contact angle between mercury and most solid materials, and *P* (Pa) is the intrusion pressure.

**Textural properties**

$H_2$, instead of $CO_2$, commonly employed for this purpose, was used to determine microporosity because $H_2$ has a smaller cross-sectional area than $CO_2$ [4]. Total pore volumes, $V_T$; volumes of pores with a diameter below 0.5 nm (not enough for a bilayer of $H_2$ molecules), $V_{<0.5\ nm}$; ultramicropore volumes (pore diameter below 0.7 nm), $V_{u\mu}$; supermicropore volumes (pore diameter between 0.7 and 2 nm), $V_{s\mu}$; and micropore volumes (pore diameter below 2.0 nm), $V_{\mu}$, were obtained by integration of the PSDs. We also used the PSDs to calculate the average pore diameters in each range of porosity considered, namely $L_0$, $L_{0<0.5\ nm}$, $L_{0u\mu}$, $L_{0s\mu}$, and $L_{0\mu}$, respectively.

**Mechanical properties**

Solid cubic samples (10 mm × 10 mm × 10 mm) with different initial tannin contents were printed, pyrolysed, and the 3D-printed carbon structure were investigated by compression tests (see experimental section). As already discussed elsewhere [5,6], the mechanical behaviour of brittle cellular materials is strongly affected by the boundary conditions. Rigidly bonding the specimens to the loading platens leads to a more homogeneous distribution of the load across the section and, consequently, to higher and much more repeatable values of modulus. Thus, the opposite faces in the *z*-direction of each cube (*i.e.*, orthogonal to the successive construction layers) were first glued with epoxy to 6 mm-thick PMMA plates, by applying a very thin layer so that the adhesive does not penetrate the porosity of the sample beyond its extreme surface. The Young's modulus, defined as the slope of the initial linear part of the curve presenting the steepest slope, and the compressive strength at break, defined as the highest point at the first stress peak, were the main mechanical parameters obtained from the obtained strain-stress curves [7].

**Table S1.** Formulation of the different acrylate-tannin resins.

| Formulation | T-10 | T-20 | T-25 | T-30 |
|---|---|---|---|---|
| CN154 [a] (wt.%) | 35.9 | 31.9 | 29.9 | 27.9 |
| PETA [b] (wt.%) | 35.9 | 31.9 | 29.9 | 27.9 |
| HDDA [c] (wt.%) | 17.9 | 15.9 | 14.9 | 13.9 |
| BAPO [d] (wt.%) | 0.3 | 0.3 | 0.3 | 0.3 |
| Tannin (wt.%) | 10 | 20 | 25 | 30 |

[a] acrylate oligomer; [b] pentaerythritol tetraacrylate; [c] hexanediol diacrylate; [d] bis(2,4,6-trimethylbenzoyl)phenylphosphine oxide

**Table S2.** Carbon yield and shrinkage of 3D-printed samples.

| Formulation | Carbon yield (%) | Shrinkage in the *z*-direction (%) | Shrinkage in the *xy*-direction (%) |
|---|---|---|---|
| T-0 | 11.7 | 40 | 30 |
| T-10 | 12.8 | 25 | 25 |
| T-20 | 14.3 | 24 | 25 |
| T-25 | 20.8 | 26 | 24 |
| T-30 | 20.9 | 26 | 24 |

**Table S3.** Chemical composition of 3D-printed carbons measured by elemental analysis (EA).

| Sample | C (wt.%) | H (wt.%) | N (wt.%) | S (wt.%) | O (wt.%)* |
|---|---|---|---|---|---|
| CT-0 | 96.3 | 1.3 | 0.3 | 0 | 2.1 |
| CT-10 | 95.2 | 1.3 | 0.3 | 0 | 3.2 |
| CT-20 | 94.3 | 1.3 | 0.5 | 0 | 3.9 |
| CT-25 | 94.8 | 1.4 | 0.3 | 0 | 3.5 |
| CT-30 | 94.7 | 1.3 | 0.5 | 0 | 3.5 |

* The oxygen content was obtained by difference

**Table S4.** Pore texture parameters of the 3D-printed carbon structures, depending on the initial tannin content.

| Sample | CT-0 | CT-10 | CT-20 | CT-25 | CT-30 |
|---|---|---|---|---|---|
| $\rho_b$ (g cm$^{-3}$) | 0.442 ± 0.016 | 0.305 ± 0.029 | 0.351 ± 0.018 | 0.404 ± 0.046 | 0.408 ± 0.019 |
| $\rho_s$ (g cm$^{-3}$) | 1.85 ± 0.04 | 1.81 ± 0.07 | 1.83 ± 0.09 | 1.85 ± 0.10 | 1.80 ± 0.07 |
| $\Phi$ (-) | 0.76 ± 0.01 | 0.83 ± 0.02 | 0.81 ± 0.01 | 0.78 ± 0.03 | 0.78 ± 0.01 |
| $A_{BET}$ (m² g$^{-1}$) | - | - | 265 | 355 | 375 |
| $S_{NLDFT}$ (m² g$^{-1}$) | - | - | 850 | 890 | 910 |
| $V_T$ (cm$^3$ g$^{-1}$) | - | - | 0.20 | 0.22 | 0.23 |
| $V_\mu$ (cm$^3$ g$^{-1}$) | - | - | 0.20 (100%) | 0.22 (100%) | 0.22 (95%) |
| $V_{s\mu}$ (cm$^3$ g$^{-1}$) | - | - | 0.05 (25%) | 0.07 (32%) | 0.07 (30%) |
| $V_{u\mu}$ (cm$^3$ g$^{-1}$) | - | - | 0.15 (75%) | 0.15 (68%) | 0.15 (65%) |
| $V_{<0.5nm}$ (cm$^3$ g$^{-1}$) | - | - | 0.13 (65%) | 0.12 (59%) | 0.13 (59%) |
| $L_0$ (nm) | - | - | 0.69 | 0.69 | 0.79 |
| $L_{0\,\mu}$ (nm) | - | - | 0.56 | 0.59 | 0.58 |
| $L_{0\,u\mu}$ (nm) | - | - | 0.43 | 0.44 | 0.43 |
| $L_{0\,s\mu}$ (nm) | - | - | 0.98 | 0.95 | 0.93 |
| $L_{0\,<0.5\,nm}$ (nm) | - | - | 0.38 | 0.37 | 0.38 |

$\rho_b$: bulk density; $\rho_s$: skeletal density; $\Phi$: overall porosity; $A_{BET}$: BET area; $V_T$: total pore volume; $V_{<0.5\ nm}$: volume of pores with a diameter below 0.5 nm (i.e., too narrow for a bilayer of $H_2$ molecules); $V_{u\mu}$: ultramicropore volume (pore diameter below 0.7 nm); $V_{s\mu}$: supermicropore volume (pore diameter between 0.7 and 2 nm); $V_\mu$: micropore volume (pore diameter below 2.0 nm). The values written in parentheses represent the volume fractions of each pore population relative to the total pore volume ($V_T$). $L_0$, $L_{0<0.5\ nm}$, $L_{0u\mu}$, $L_{0s\mu}$, and $L_{0\mu}$ are average pore diameters in each range of porosity considered, respectively.

**Table S5.** Electrical conductivity of the pyrolysed 3D-printed structures, depending on the initial tannin content

| Sample | Electrical conductivity ($S \cdot cm^{-1}$) | Estimated skeleton conductivity ($S \cdot cm^{-1}$) |
|---|---|---|
| CT-0 | 7.05 | 44.50 |
| CT-10 | 6.05 | 58.94 |
| CT-20 | 7.03 | 58.54 |
| CT-25 | 6.77 | 47.91 |
| CT-30 | 6.38 | 43.13 |

**Table S6.** Main mechanical properties of 3D-printed carbons in this study

| Sample | Compressive strength (MPa) | Strain at break (%) | Young's modulus (MPa) |
|---|---|---|---|
| CT-0 | 2.89 ± 0.08 | 4.9 ± 0.1 | 155.62 ± 0.80 |
| CT-10 | 1.42 ± 0.08 | 7.0 ± 0.1 | 83.21 ± 0.52 |
| CT-20 | 1.60 ± 0.06 | 5.2 ± 0.5 | 93.71 ± 0.62 |
| CT-25 | 1.86 ± 0.03 | 2.9 ± 0.3 | 153.05 ± 1.80 |
| CT-30 | 1.68 ± 0.04 | 2.7 ± 0.2 | 149.77 ± 2.79 |

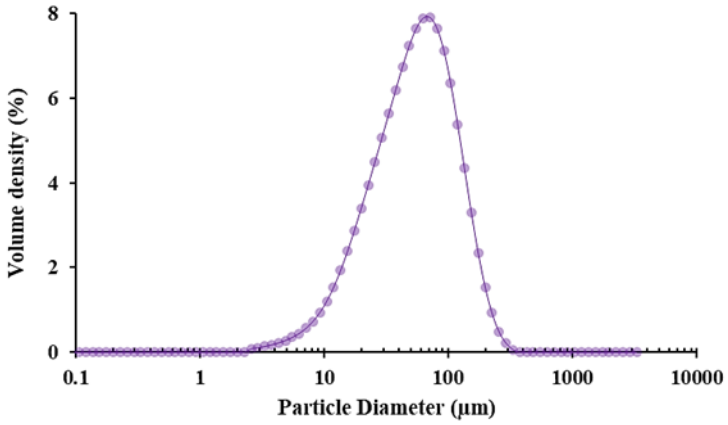


**Figure S1.** Volume-based particle size distribution of mimosa (*Acacia Mearnsii*) tannin powder obtained with the Malvern Mastersizer. Each dot is an average of three replicates.

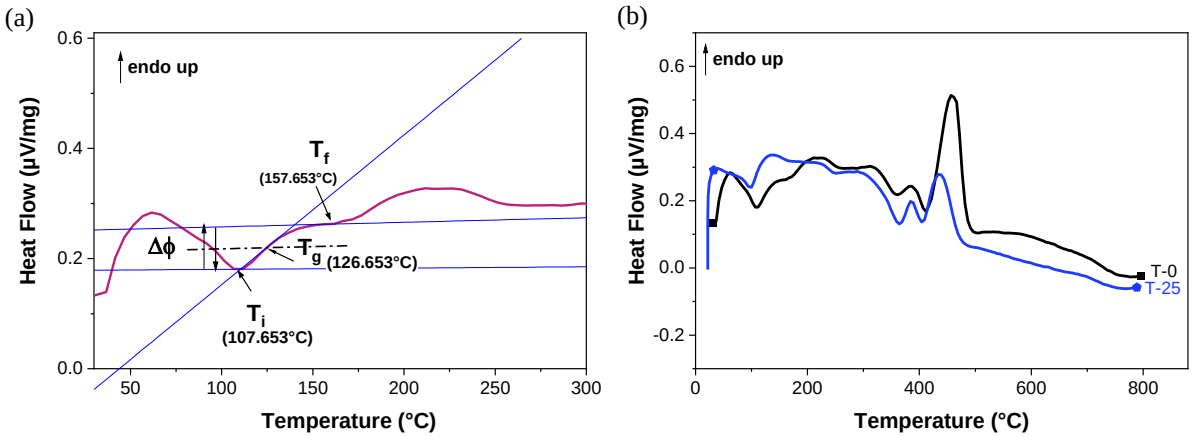


**Figure S2.** (a) DSC thermogram of T-0 resin, showing the glass transition temperature $T_g$; (b) DSC thermogram of T-0 and T-25 resins.

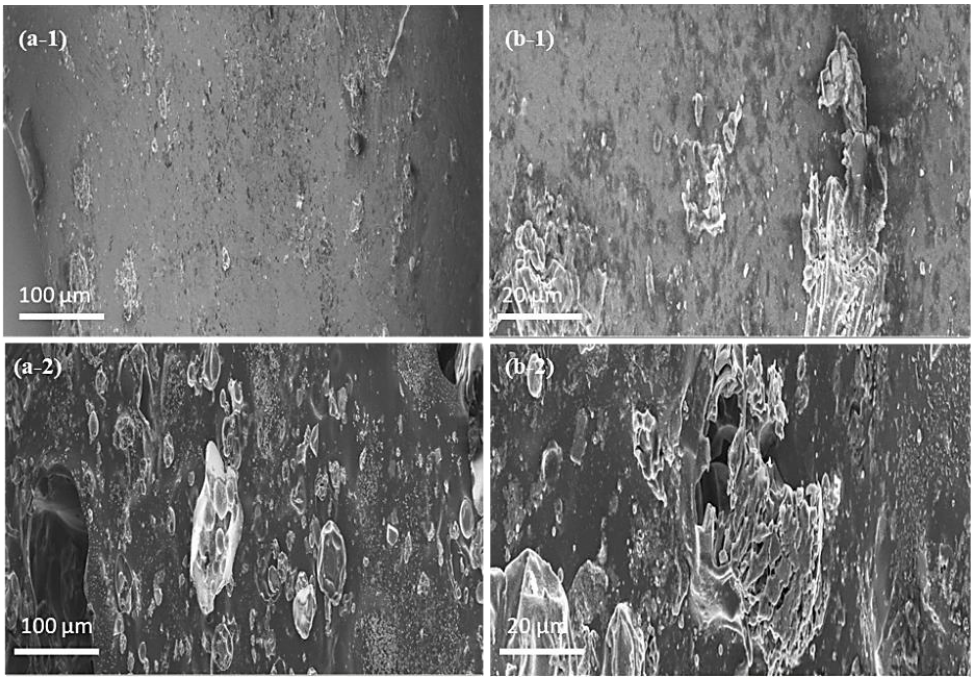


**Figure S3.** SEM images of the outer surface of 3D-printed structures pyrolysed at 900°C made from: (1) unfilled resin; (2) resin with 30 wt.% of tannin. Scale bars: (a) 100 μm; (b) 20 μm.

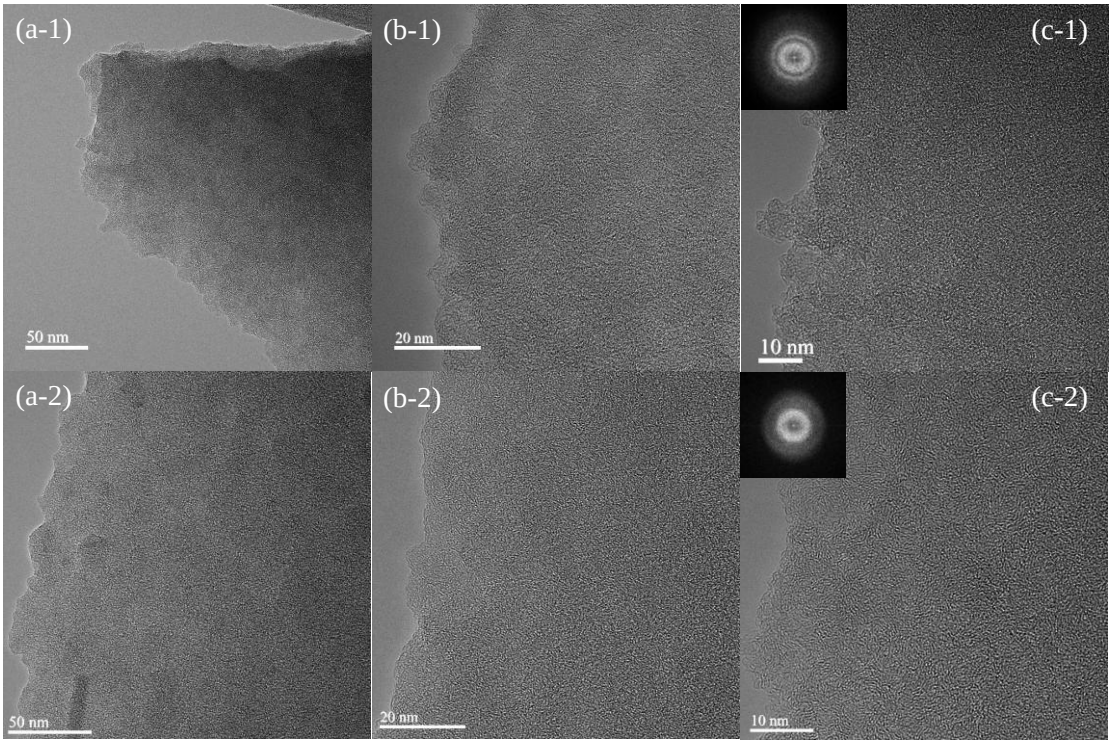


**Figure S4**. (a,b) Bright-field; and (c) high-resolution TEM images at different magnifications of 3D-printed carbon structures prepared from: (1) pristine resin; and (2) resin loaded with 30 wt.% of tannin. Scale bars: (a) 50 nm; (b) 20 nm; (c) 10 nm.

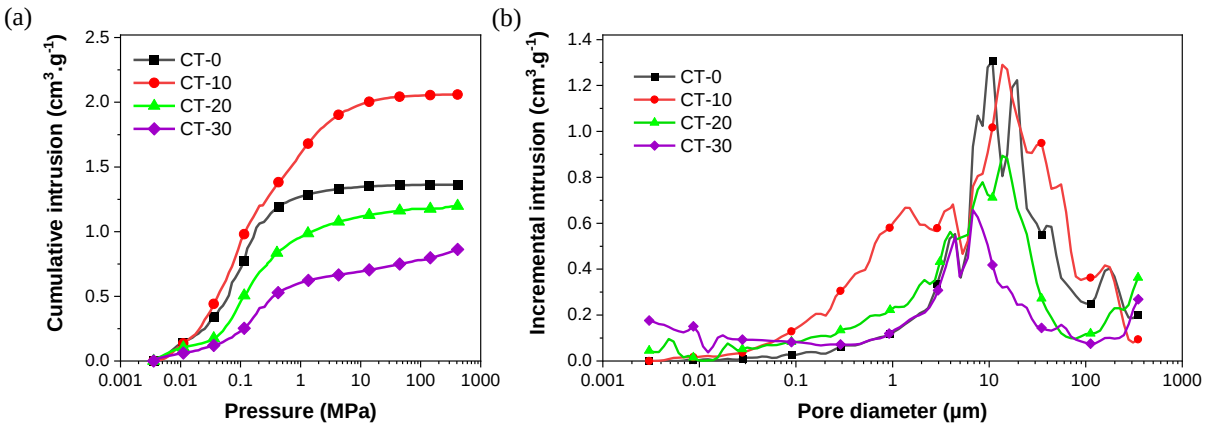


**Figure S5.** Results of mercury porosimetry: (a) raw intrusion curves; (b) corresponding pore size distributions calculated from Eq. (5).

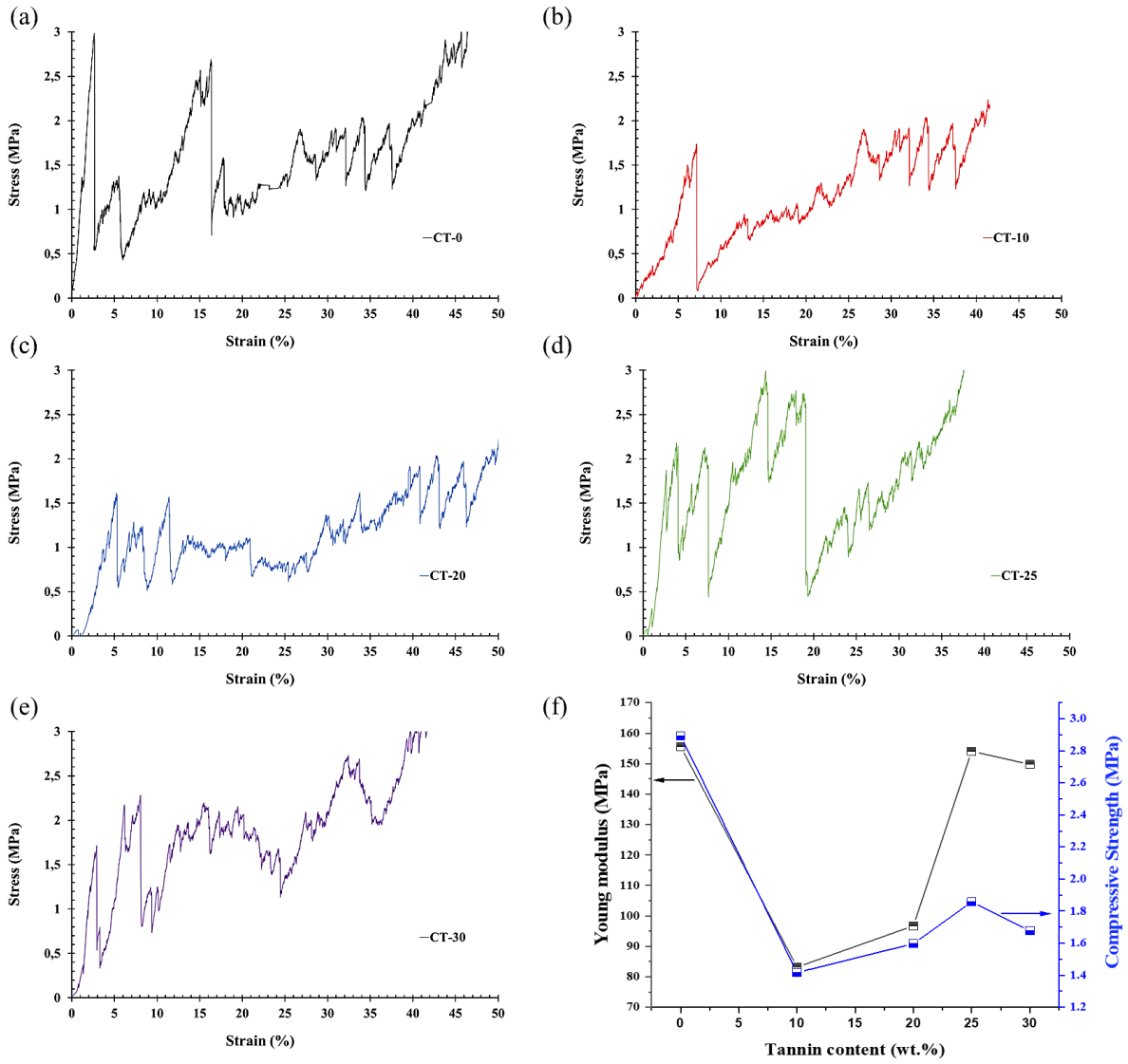


**Figure S6.** Stress-strain characteristics of the 3D-printed carbon structures submitted to uniaxial, quasi-static compression: (a) CT-0; (b) CT-10; (c) CT-20; (d) CT-25; and (e) CT-30 samples. (f) Modulus and strength of 3D-printed carbons as a function of initial tannin content in the resin: some error bars are barely noticeable although they are present in the graph.

REFERENCES


(1) Bernard, S.; Beyssac, O.; Benzerara, K.; Findling, N.; Tzvetkov, G.; Brown, G. E. XANES, Raman and XRD Study of Anthracene-Based Cokes and Saccharose-Based Chars Submitted to High-Temperature Pyrolysis. *Carbon* **2010**, *48* (9), 2506–2516. https://doi.org/10.1016/j.carbon.2010.03.024.

(2) Szczurek, A.; Fierro, V.; Medjahdi, G.; Celzard, A. Carbon Aerogels Prepared by Autocondensation of Flavonoid Tannin. *Carbon Resources Conversion* **2019**, *2* (1), 72–84. https://doi.org/10.1016/j.crcon.2019.02.001.

(3) Mallet-Ladeira, P.; Puech, P.; Toulouse, C.; Cazayous, M.; Ratel-Ramond, N.; Weisbecker, P.; Vignoles, G. L.; Monthioux, M. A Raman Study to Obtain Crystallite Size of Carbon Materials: A Better Alternative to the Tuinstra–Koenig Law. *Carbon* **2014**, *80*, 629–639. https://doi.org/10.1016/j.carbon.2014.09.006.

(4) Jagiello, J.; Kenvin, J.; Ania, C. O.; Parra, J. B.; Celzard, A.; Fierro, V. Exploiting the Adsorption of Simple Gases O2 and H2 with Minimal Quadrupole Moments for the Dual Gas Characterization of Nanoporous Carbons Using 2D-NLDFT Models. *Carbon* **2020**, *160*, 164–175. https://doi.org/10.1016/j.carbon.2020.01.013.

(5) Brezny, R.; Green, D. J. Uniaxial Strength Behavior of Brittle Cellular Materials. *J American Ceramic Society* **1993**, *76* (9), 2185–2192. https://doi.org/10.1111/j.1151-2916.1993.tb07753.x.

(6) Mora, R. J.; Waas, A. M. Strength Scaling of Brittle Graphitic Foam. *Proc. R. Soc. Lond. A* **2002**, *458* (2023), 1695–1718. https://doi.org/10.1098/rspa.2001.0938.

(7) Celzard, A.; Zhao, W.; Pizzi, A.; Fierro, V. Mechanical Properties of Tannin-Based Rigid Foams Undergoing Compression. *Materials Science and Engineering: A* **2010**, *527* (16–17), 4438–4446. https://doi.org/10.1016/j.msea.2010.03.091.